Measuring Elemental Abundances in Metal-Poor Stars

Undergraduate Research Thesis

Presented in Partial Fulfillment of the Requirements for graduation *with research distinction* in Astronomy in the undergraduate colleges of The Ohio State University

By

Jared Kolecki

The Ohio State University

December 2020

Project Advisors: Dr. Ji Wang & Dr. Jennifer Johnson, Department of Astronomy

Draft version December 3, 2020

Typeset using LaTeX **preprint** style in AASTeX63

ABSTRACT

By analyzing the elemental abundance profile of a star, insight can be gained into the composition of its initial dust cloud. Using this insight, it is possible to determine the likelihood that the star was able to form planets based on the amount of metal material available. We present an analysis of 16 dwarf stars in the galactic halo, a relatively metal-poor region when compared to the thin disk, where most currently known exoplanets reside. We calculated detailed elemental abundance profiles for each of these stars and found their metallicities to be in the range expected for halo stars (-2.0 $\leq$ [Fe/H] $\leq$ -0.5). In this process, we also determined the values of the effective temperature and surface gravity for each star.

1. INTRODUCTION

A planet-metallicity correlation has been well-demonstrated for gas giant planets across a wide range of stellar metallicities. If a star is metal-rich, it is more likely to have formed giant planets. The accepted theory explaining the cause of this correlation is as follows: In order for a star to form planets, the initial dust cloud needs to be rich enough with metals (the key component of dust particles and the amalgamations thereof, i.e. planets) that the particles are sufficiently dense and numerous enough to be able to coalesce to form larger particles, which then form planetesimals which can accrete gas around them and create a gas giant. Thus, if the cloud is too metal-poor, this accretion will not happen on a large enough scale to form particles big enough that they grow to become planets.

This same correlation, however, has not been firmly established for terrestrial planets. This is an important problem to tackle as it has implications regarding target selection for future exoplanet searches. If terrestrial planets are indeed more common around metal-rich host stars, these stars should be prioritized for observation. Conversely, if it can be determined that, below a certain stellar metallicity, the probability that a terrestrial planet forms approaches 0, stars of and below that threshold can be safely removed from target samples in order to conserve observation time for more interesting targets.

We performed a spectroscopic abundance analysis on stars selected from a larger set of dwarf halo stars. These stars were especially chosen as good candidates for being metal-poor, and have been selected for observation by TESS to confirm the presence of any detectable transiting planets orbiting them. Additionally, as most currently-discovered exoplanets reside in the galactic thin-disk, this analysis hopes to provide some insight into planet formation in areas of the galaxy with different chemical makeup and stellar populations.

Finally, the halo contains some of the oldest stars in the Milky Way. This analysis will allow more insight into the correlation between planet formation and metallicity in this domain, as well provide information that will help us to understand an area of our galaxy which preserves important information on the formation and earliest chemical evolution of our galaxy (Bullock & Johnston 2005).

Until recently, however, it has not been easy to identify halo stars. Even the distribution of their ages has not been fully understood. The Gaia mission (Gaia Collaboration et al. 2016) though, has the identification process can be made far more efficient through its astrometry and radial velocity measurements of one billion stars in the Milky Way.

2. SAMPLE SELECTION

2.1. *Larger Dwarf Sample*

For the purposes of our analysis, the sample selection should be such that the stars within it have a high probability of being metal-poor. Since the solar neighborhood is composed of roughly 1%

metal-poor stars, we must look elsewhere for a metal-poor sample of sufficient purity. The galactic halo is a region that is known to contain a significant fraction of metal-poor stars, so our selection criteria were centered around values that would be characteristic of stars in this region. This selection process used kinematics data from Gaia, as well as stellar radius data from $\mathrm{CTLv08}_{01}$ (Stassun et al. 2018, 2019) to limit the sample to dwarf stars. In the end, 17,342 stars were selected, and we estimate the success rate of selecting dwarf halo stars to be approximately 70%.

To confirm this, we can analyze the demographics of the sample to confirm that they are within expectations. Figure 1a displays the distribution of stellar radii in the sample and shows that the peak of the distribution falls at approximately 0.7 $\mathrm{R}_{\odot}$. Figure 1b shows the distance distribution of the sample, which was chosen so that all stars selected have $d < 1\,\mathrm{kpc}$. Regarding Figure 1c, Casey et al. (2018) shows a metallicity correlation with a star's $(W1 - W2)$ color index. Specifically, their results suggest that selecting a sample of stars with $-0.05 \leq (W1 - W2) \leq 0.05$ increases the yield of metal-poor stars (defined as having $[\mathrm{Fe/H}] \leq -1.5$) significantly over the results of a random selection by a factor of 250. Since the majority of stars we selected fall within this color range, we can use this to conclude that we have a high chance of finding that our sample is largely metal poor. The discontinuous distribution of $Tmag$ displayed in Figure 1d is due to the fact that although the majority of targets from the CTL have $T < 13$, the Cool Dwarf list extends to $T = 16$ (for a description of this special list, see Muirhead et al. 2018).

2.2. *Detailed Subsample*

16 stars were chosen that were either taken directly from the larger sample, or were shown to have properties fitting the expected demographics. In particular, we took Gaia kinematics data for each star and used the method outlined in Johnson & Soderblom (1987) to calculate galactic space velocities, ensuring that the results were indicative of stars in the galactic halo ($|v| > 200\,\mathrm{km\,s^{-1}}$). We also did the same for all the stars in the larger halo sample with Gaia radial velocity data. The results are displayed in Figure 2, which shows that all of the stars exhibit halo-like kinematics. The diagram is a projection of a star's 3-dimensional space velocity onto a 2-dimensional plane, where

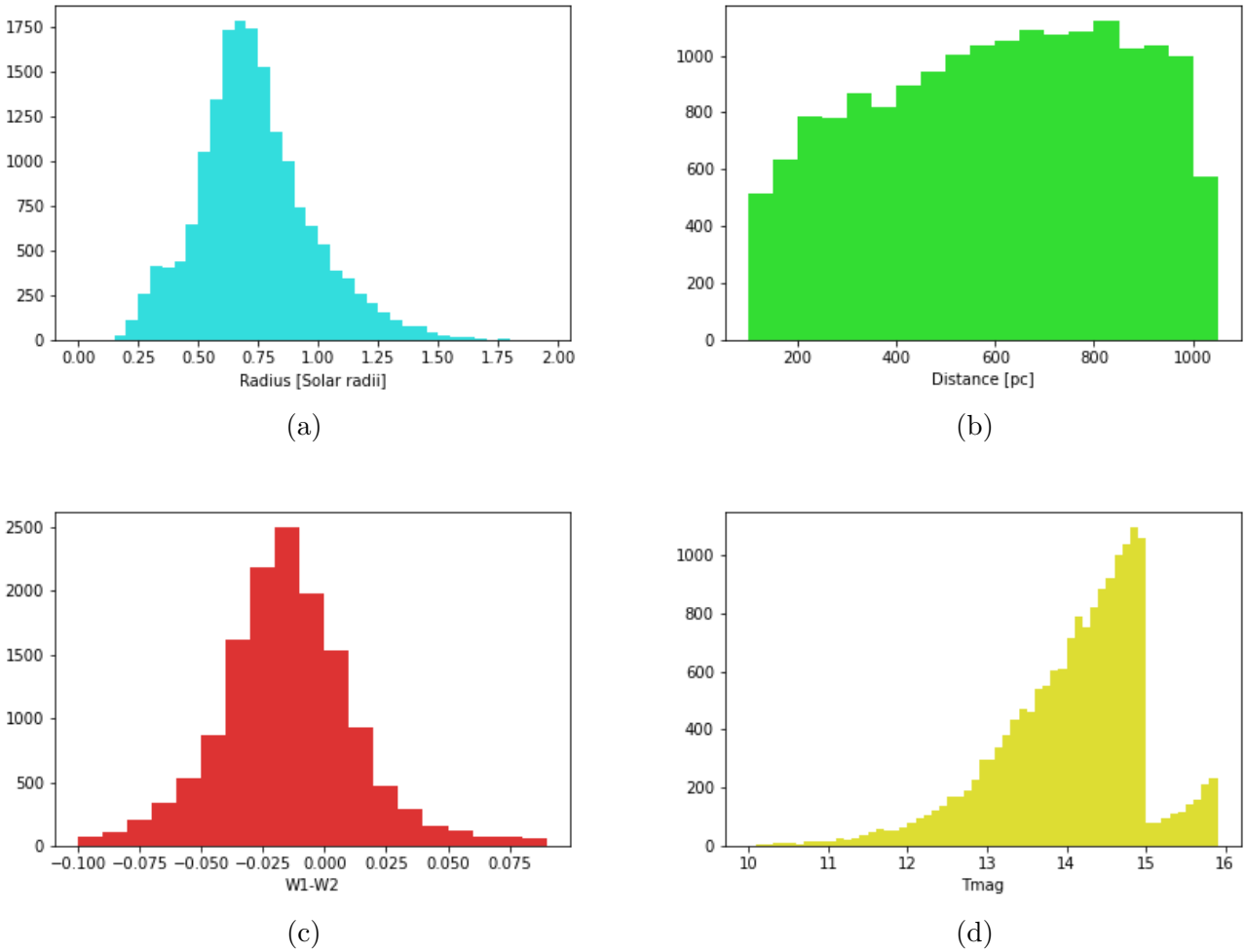

(a) (b)

(c) (d)

Figure 1: Demographics of the Halo Sample

the x-axis represents velocity in the direction of galactic rotation (V), and the y-axis represents the magnitude of the vector sum of radial velocity (U) and velocity perpendicular to the galactic plane (W). A star's total velocity is represented by its distance from the origin. For this reason, isovelocity lines are shown in gray for readability.

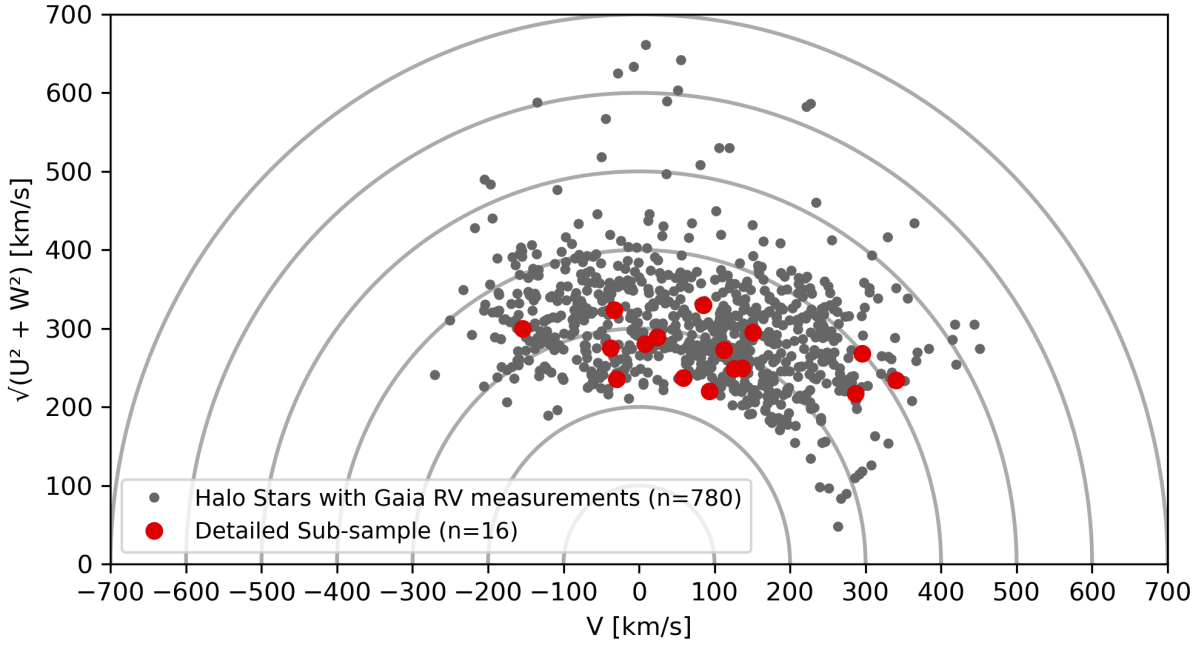

Figure 2: Galactic Space Velocities of the Sample With Respect to the Local Standard of Rest

3. ABUNDANCE ANALYSIS

3.1. *PEPSI Spectra*

Observations of each of these stars were taken using the Large Binocular Telescope's PEPSI high-resolution spectrograph. The resulting data was fed through a reduction pipeline to create merged 1-dimensional spectra in both the R band and the B band.

In order to derive stellar parameters and abundance profiles of the stars, we first calculated the equivalent widths of the absorption lines from elements of interest. We did this using a custom Python program which allowed us to adjust the continuum and wavelength range over which to calculate the equivalent widths to get precise measurements. Examples of the resulting plots and calculations can be found in Figure 4, which shows Iron I line features of varying strengths. In the plots, the line feature is drawn in gray, the continuum in dark blue, and the minimum point of the line feature in light blue. The dark blue lines on either side of the minimum point are a graphical depiction of the equivalent width, which is shown in units of mÅ. Absorption lines and their relevant data were chosen from Table 3 of Fulbright (2000).

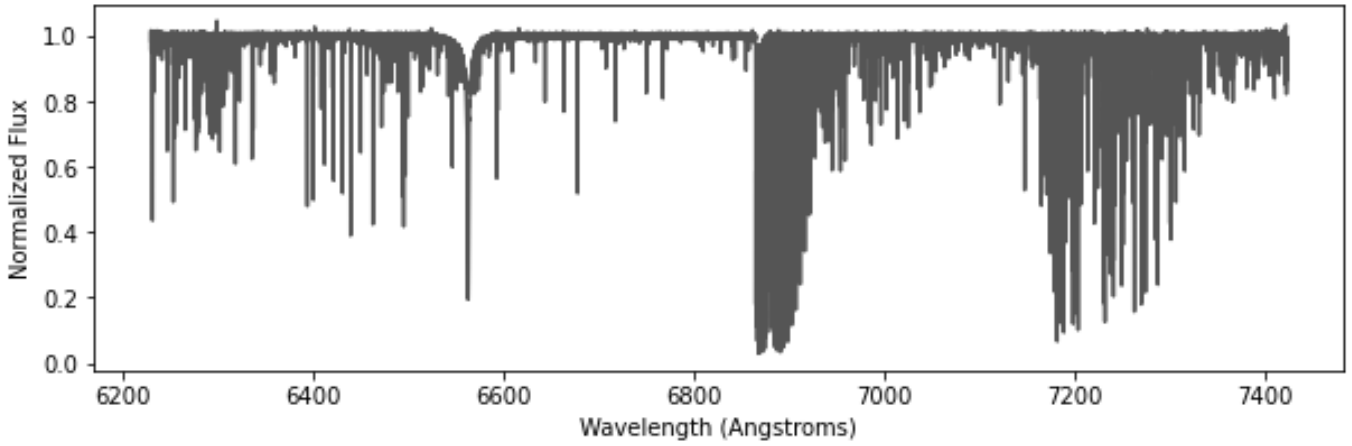

Figure 3: Example of Reduced 1-Dimensional Spectra: The R-band Profile of BD+51 1696.

Once we had calculated equivalent widths for each star, we chose to keep only lines which had equivalent widths greater than 5 mÅ. This was due the signal-to-noise ratio of the spectra preventing any accurate measurement of weaker absorption lines, which is best illustrated by comparing Figure 4d to

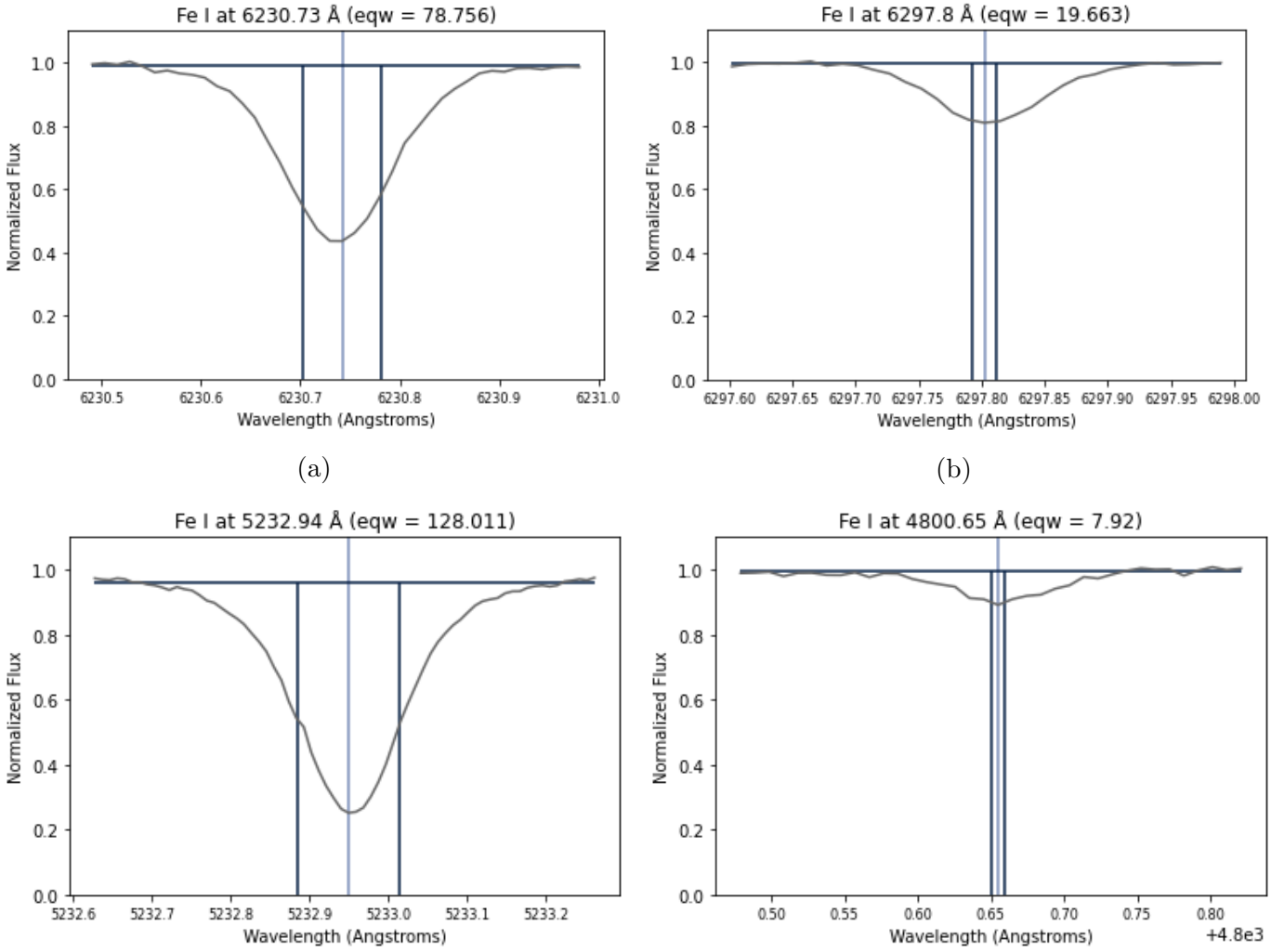

Figure 4: Example Results of Equivalent Width Calculation on BD+51 1696

the other plots in the figure. For certain stars, this resulted in no usable line strength measurements for a given element. In this case, we simply ignored that element in our analysis (represented as "–" in our final abundance results, which can be viewed in Table 3).

Table 3 of Fulbright (2000) conveniently contains wavelength, excitation potential, and oscillator strength data for every spectral line listed. We took this data and combined it with our equivalent width data to produce unique line lists for each star. In our analysis, we used PyMOOGi[1] (Adamow 2017), a Python implementation of the Fortran code MOOG[2] (Sneden 1973), which itself is a popular

[1] https://github.com/madamow/pymoogi
[2] http://www.as.utexas.edu/~chris/moog.html

tool in stellar spectroscopy. MOOG also requires model stellar atmospheres. We used ODFNEW model atmospheres from Kurucz's grids[3] and the KMOD interpolation tool[4] to create appropriate atmospheres which closely matched our stars

3.2. *The Abundance Analysis Process*

MOOG is a spectral analysis tool widely used for line analysis and synthesis. In our analysis we used the driver `abfind`, which uses the basic equations of LTE spectral line analysis to fit chemical abundances to an input line profile given an appropriate model stellar atmosphere. In order to get appropriate atmospheres, we first needed to get accurate stellar parameters, which for our needs include T_{eff} , log(g), microturbulence (ξ), and [Fe/H]. Details on the methods we used to determine these parameters can be found in the following section, 3.3. At this point, using the model atmosphere grids from Kurucz, we were able to use KMOD to linearly interpolate models that closely fit each star. Then, we ran our model atmospheres and line lists through MOOG, which outputs a summary file, and a plot for each element.

The summary output file contains statistics which detail the mean abundance calculated from each line of the elements in the line list, along with the standard deviation. Figure 5 is an example of one of the graphs output by MOOG, where in this case, neutral Iron is plotted in blue and singly-ionized Iron is plotted in green. The individual abundances derived from each line are plotted as points, and the average abundance is represented by the horizontal dashed line. The solid lines are trend lines of abundances in each of their respective parameter spaces, useful for obtaining accurate stellar parameters while assuming local thermodynamic equilibrium, which requires that the slope of some of these trend lines be equal to 0 within a margin of error. While we first attempted a strict LTE assumption, in our final analysis, we decided to forego this. This yielded more consistent results when fitting the sample subset to stellar isochrones in different parameter spaces from the Dartmouth Stellar Evolution Pipeline. More details can be found in Section 4.1.

[3] http://kurucz.harvard.edu/grids.html
[4] http://www.as.utexas.edu/~hebe/stools/

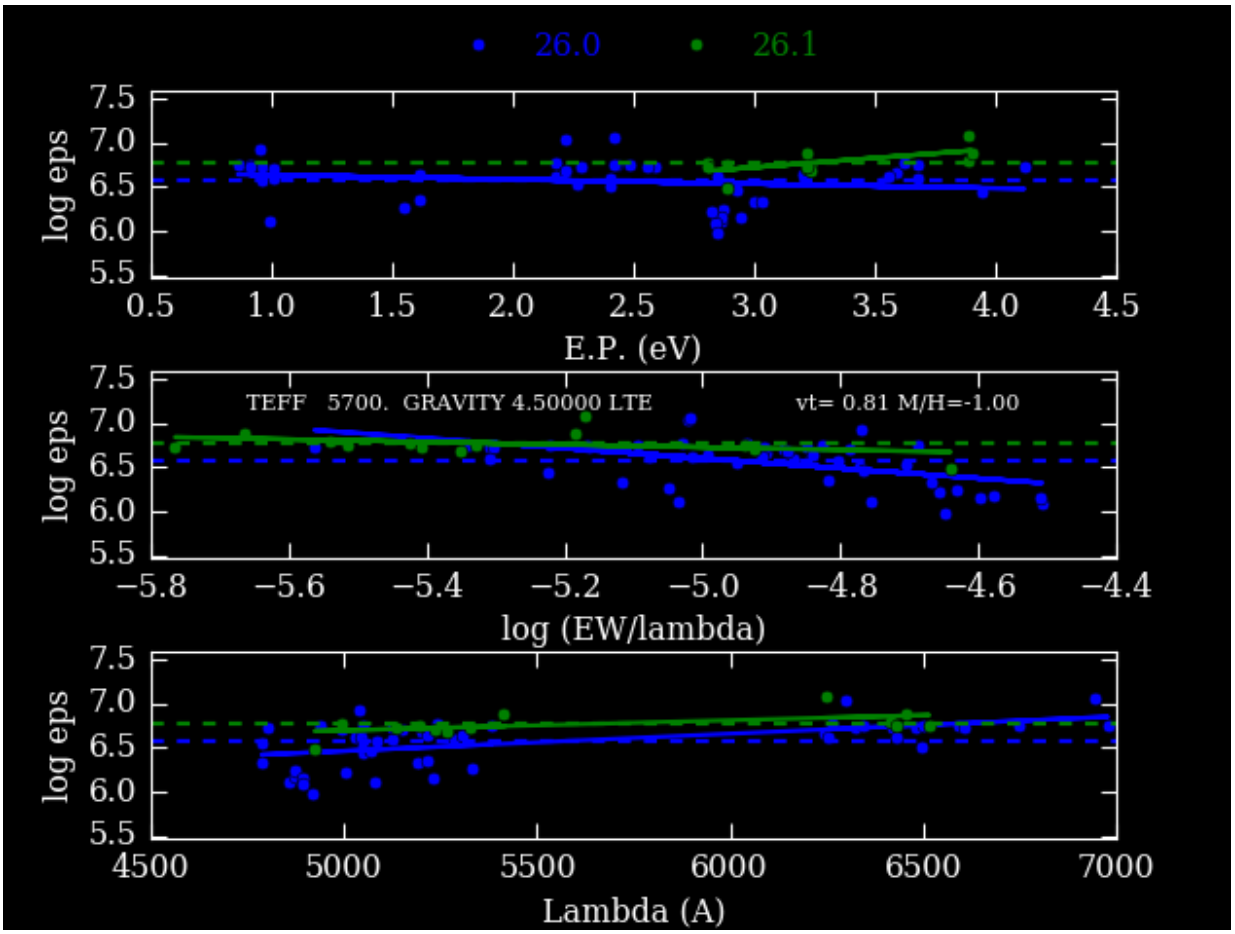

Figure 5: Example MOOG Output Graph: The Iron abundance profile of star TYC 3873-597-1

3.3. *Stellar Parameter Derivation*

We report T_{eff} to a precision of 10 K, surface gravity to a precision of 0.05 $\log(\mathrm{cm\,s^{-2}})$, and microturbulence to a precision of 0.01 $\mathrm{km\,s^{-1}}$. These values, along with the error associated with them, are displayed in Table 2.

3.3.1. *Effective Temperature and Surface Gravity*

Since all 16 stars have Gaia photometry and 2MASS photometry publicly available through the Gaia archive and SIMBAD, we used spectral colors calculated from this photometry to compare against the Dartmouth isochrones to develop new parameters.

This was a two-part process. Initially, we compared each star's photometry against the isochrone for a 10 Gyr old population with [Fe/H] = -1.0. Color comparisons were done using every combination

of band magnitudes available (G, Bp, and Rp from Gaia, and J, H, and K from 2MASS). Each individual color corresponded to a specific evolutionary stage along the isochrone, which carries with it values for T_{eff} and log(g). The median value of both over all possible colors were taken to be our first approximation of effective temperature and surface gravity. We chose to use the median instead of the mean due to the occasional significant outlier in the data. A tabled example of the results of this process for one of our stars is found in Table 1.

Color Index	T_{eff} [K]	log(g [cm s^{-2}])
(G - Rp)	6200	4.40
(G - Bp)	5930	4.55
(Bp - Rp)	6090	4.50
(J - H)	6380	4.05
(H - K)	5610	4.60
(J - K)	6220	4.40
(G - J)	6170	4.45
(G - H)	6220	4.40
(G - K)	6170	4.45
(Bp - J)	6090	4.45
(Bp - H)	6170	4.45
(Bp - K)	6130	4.45
(Rp - J)	6130	4.45
(Rp - H)	6230	4.40
(Rp - K)	6170	4.45
MEDIAN	6170	4.45

Table 1: Example of Photometric Derivation of T_{eff} and log(g) For HD 108177

We then took these parameters and ran them through MOOG, determining an initial Fe metallicity for the star. With this [Fe/H] value, along with the star's position on the $(G - Rp)$ color versus G magnitude diagram to determine an approximate age, we were able to get a new, more accurate isochrone for the star to fall on. The process of comparing the star's spectral colors was repeated once more using this new isochrone, and we took the resulting T_{eff} and log(g) values to be used in our analysis. In theory, this process could be iterated further. However, the values resulting

from any second-order correction were found to be within one standard deviation of the first-order approximation, making this a negligible correction.

3.3.2. *Microturbulence*

To determine a value for the microturbulence parameter, we used Iron I lines of similar excitation potential and varying equivalent widths to remove the correlation between equivalent width and derived abundance by varying the microturbulence parameter. This resulted in about five Fe I lines for each star being used for this process. Our reasoning for limiting the Iron lines used was such that we were able to minimize non-LTE effects. Since MOOG assumes LTE, using a range of lines with different excitation potentials would expose this calculation to uncertainties stemming from the fact that the star is not in excitation equilibrium since we did not derive T_{eff} spectroscopically.

Star	T_{eff} [K]	log(g [cm s^{-2}])	ξ [km s^{-1}]
BD+18 3309	5710 ± 80	4.60 ± 0.06	0.83 ± 0.44
BD+18 3423	5960 ± 70	4.40 ± 0.17	0.71 ± 0.10
BD+20 2594	5980 ± 70	4.55 ± 0.06	0.67 ± 0.12
BD+20 3603	6270 ± 40	4.45 ± 0.12	0.64 ± 0.18
BD+25 1981	6860 ± 90	4.40 ± 0.08	1.67 ± 0.31
BD+34 2476	6270 ± 40	4.40 ± 0.11	0.66 ± 0.17
BD+36 2165	6160 ± 50	4.40 ± 0.10	0.50 ± 0.22
BD+42 2667	5980 ± 30	4.55 ± 0.03	0.94 ± 0.31
BD+51 1696	5670 ± 60	4.60 ± 0.05	0.53 ± 0.38
BD+72 659	4440 ± 30	4.55 ± 0.01	1.02 ± 0.16
BD+75 839	5710 ± 30	4.55 ± 0.03	1.10 ± 0.13
HD 64090	5450 ± 40	4.70 ± 0.02	1.07 ± 0.40
HD 108177	6170 ± 40	4.45 ± 0.11	0.73 ± 0.26
HD 160693	5790 ± 60	4.45 ± 0.11	1.29 ± 0.24
HD 194598	6040 ± 50	4.50 ± 0.05	1.17 ± 0.23
TYC 3873-597-1	5700 ± 30	4.50 ± 0.03	0.83 ± 0.12

Table 2: Stellar Parameters

3.4. *Error Analysis*

For stellar parameters, errors on T_{eff} and log(g) were calculated as the standard deviation of the mean value taken from the isochrones as explained in the previous section. Uncertainty in the microturbulence parameter was determined by varying the microturbulence by 0.1 km/s and relating the the change in ξ to the change in metallicity using the equation $\sigma_\xi = \frac{\sigma_{[Fe/H]}}{M_f - M_i}(0.1km/s)$ where M_i is the Iron I abundance derived from using ξ, and M_f is the Iron I abundance derived using $\xi + 0.1km/s$ as the microturbulence parameter.

For elemental abundances, the error was taken to be the standard deviation of the mean abundance derived by MOOG. For the case where a star had only one usable spectral line for a given element, we took the average error of the same element's abundance from other stars of similar parameters. For elements which only had at maximum one usable spectral line per star (This includes Li, V, Ba, and Eu), we chose to vary the continuum used to calculate the equivalent width, using the 'eye test' to find an upper and lower bound on it. We then ran PyMOOGi on both these parameters and took the average deviation of the two to be the standard deviation of the abundance. This yielded consistent results from star to star, which suggests that this method is valid. However, because of the inherent uncertainty in using this method, we report standard deviations calculated this way to only two significant figures.

3.5. *Results*

We found the stars to fall within ranges of $4400 \leq T_{eff} \leq 6900$, $4.4 \leq log(g) \leq 4.7$, and $-2.0 \leq$ [Fe/H] ≤ -0.45. We take the [Fe/H] parameter to be equal to the Fe II abundance rather than Fe I as a consequence of our choice to forego ionization balance as we do not assume LTE. This is because Fe II lines are significantly less affected by the consequences of this when run through MOOG (which assumes LTE in its equations) than Fe I lines. These ranges confirm the assumptions of the selection process that these stars are indeed metal-poor dwarfs. Complete abundance data and errors can be found in Table 3. We used solar abundance values from Palme et al. (2014) to transform our results to be relative to solar.

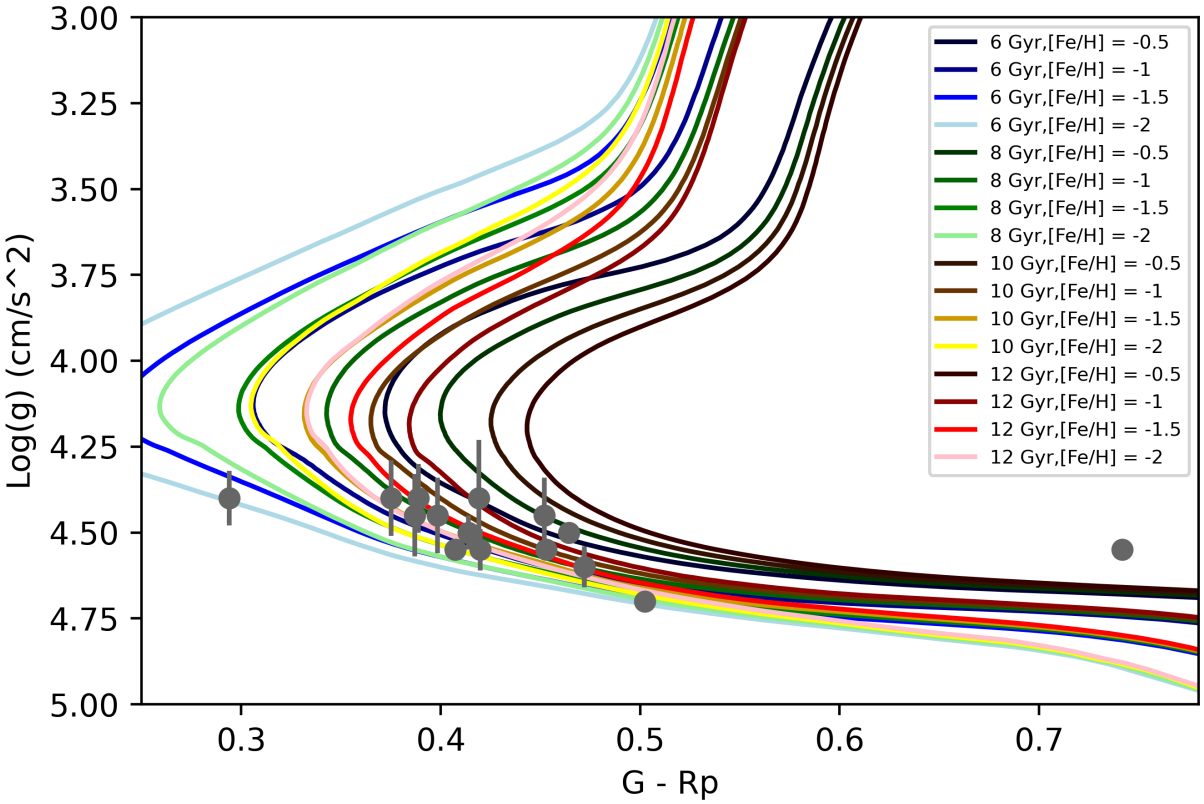

Figure 6: Color-Log(g) Diagram of the Sample

We can show the validity of our parameter choice, as well as show that the stars are indeed metal-poor, by plotting the stars on an HR diagram along with isochrones of relevant age and metallicity. Figure 6 displays the results of this, with several isochrones covering the range of the sample parameters. These isochrones have been assigned (arbitrarily and for clarity purposes) color corresponding to the age of the stellar population they represent, and lightness corresponding to their representative metallicity. The gray points represent our 16 sample stars, which fit nicely into the main sequence section of the isochrones from $-2.0 \leq [\mathrm{Fe/H}] \leq -0.5$ and $6\,\mathrm{Gyr} \leq \mathrm{Age} \leq 12\,\mathrm{Gyr}$. The notable outlier from this conformity is the star BD+72 659, with $(G - Rp) > 0.7$, which sits firmly above the highest-metallicity isochrones in the diagram. This can be attributed to its large [Fe/H] error ($[\mathrm{Fe/H}] = -0.477 \pm 0.242$), which cannot be adequately quantified in this parameter space.

To further confirm the validity of our results, Figure 7 displays a comparison of two cumulative metallicity distributions. The first, plotted in gray, is a cross-referencing of the larger, 17,342-star sample with stars in APOGEE DR14 that have metallicity data available. The resulting subset contains 118 halo stars with APOGEE metallicity data. In red is plotted the distribution of metallicity we derived from our smaller 16 star sample. This falls well within the range of the expected distribution, further backing up the validity of our results.

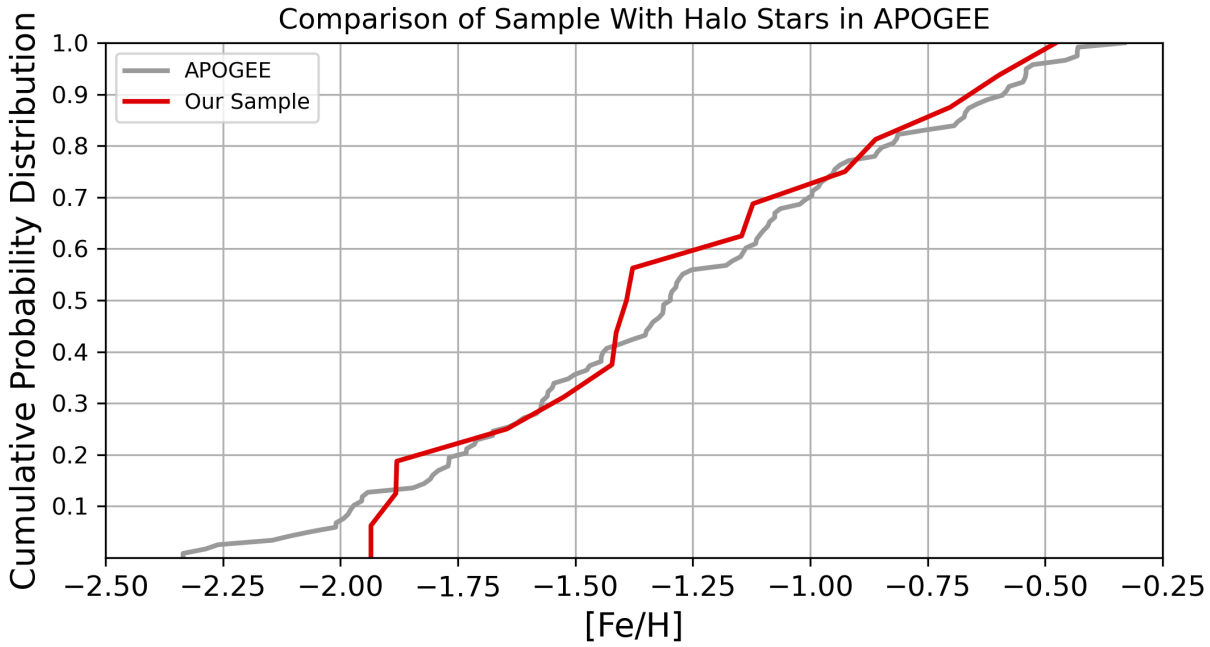

Figure 7: Cumulative Metallicity Distribution Comparison

4. DISCUSSION

4.1. *Analysis Methods*

Originally, we performed our analysis assuming that the stars were in a state of local thermodynamic equilibrium (LTE). Under this assumption, stellar parameters can be determined purely using the spectroscopy. This is done by adjusting the following parameters accordingly until certain conditions are met:

1. Effective Temperature: The star should be in excitation equilibrium, i.e. the correlation between abundance derived from each line and excitation potential should be removed.

2. Surface Gravity: The star should be in ionization balance, i.e. the abundances of Fe I and Fe II should be within error the same.

3. Microturbulence: The correlation between abundance derived from each line and reduced equivalent width ($log(\frac{\mathrm{eqw}}{\lambda})$) should be removed.

Normally, convergence of these three criteria would be good enough to accept the resulting parameters as correct, especially as selecting a set of parameters which satisfied all three of the above conditions proved to be very difficult in some cases. However, our results, particularly those for surface gravity, did not match up with what was expected. The larger sample we selected our stars from was chosen specifically to contain dwarf stars. However, our initial log(g) range placed the stars in a section of the color-log(g) plane where, based on theoretical isochrones, sub-giant stars would be found after they've evolved off the main sequence. This did not agree with their positions on the color-magnitude plane, which were indicative of main-sequence dwarfs, as illustrated in Figure 8. On the left, our sample is plotted using our log(g) values derived under the LTE assumption. On the right are the same stars on a color-magnitude diagram. Both sets are plotted along with the same isochrones as were used in Figure 6. This makes it easier to show the significance of the initial discrepancy in our initial results versus what we expected based on other data about the stars. These original surface gravity values were also accompanied by very large errors, which were rectified in our final analysis, as illustrated in Figure 6. This, along with the discrepancies we found with Reddy et al. (2006), led us to use photometry to derive the stellar parameters rather than our spectroscopy, which produced results more in line with expectations given the population demographics of our sample.

4.2. *Comparison*

We found 6 stars in common with Reddy et al. (2006), which had also performed a similar abundance analysis. Their method involved deriving T_{eff} photometrically using both (b - y) and (V - K), except in the case where this resulted in a deviation of $\sigma(T_{\mathrm{eff}}) > 69K$. In this case, T_{eff} was derived

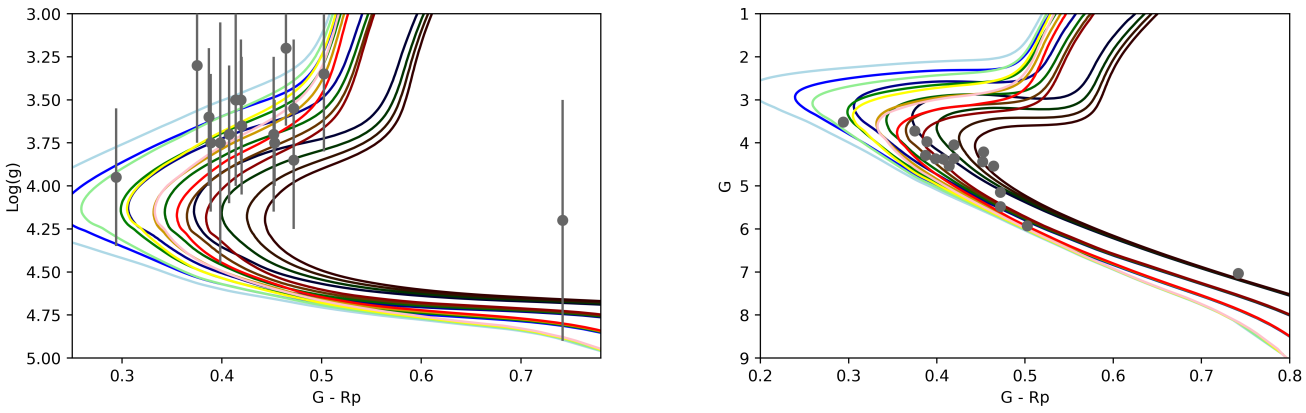

(a) (b)

Figure 8: Our Initial Log(g) Values Plotted on a Color-Log(g) Graph, Constrasting with a Color-Magnitude Diagram of the Same Stars

spectroscopically. Their method of deriving log(g) was fundamentally the same as that which we employed, though they used separately derived isochrones, in conjunction with Hipparcos data.

Though our spectroscopic temperatures were within 5% of their values for the same stars, the discrepancy between our initial log(g) values and those which they derived was in some cases roughly an entire order of magnitude. This problem was solved once we re-derived our surface gravities photometrically, which led to much better agreement between the papers.

In addition to Reddy et al. (2006), we also compared our results with those of Boesgaard et al. (2011), with which we found 7 stars in common. In this paper, they described a stellar parameter determination process very similar to our original spectroscopic method. Our metallicities derived from this method were within 0.2 dex of their derivations. However, when we re-determined our stellar parameters more accurately, the mean Iron abundance of our sample subset was raised by 0.345 dex. This fact leads us to believe that the biggest source of error among studies on these stars is whether or not the stellar parameter determination process assumes LTE.

The conclusion that can be drawn from these comparisons is that great care must be taken to ensure consistency among the implications of the stellar parameters one has chosen. Otherwise there is a risk of converging on incorrect values which then lead to incorrectly-derived abundances.

5. CONCLUSION

Using this metallicity data we've obtained, we can predict the viability of the stars in our sample for hosting planets. Figure 9 illustrates one method of doing so, making the assumption that all stars begin within a dust cloud of similar mass to that which formed the solar system, or about 30 Earth masses worth of material. Using this initial condition, we can show what the minimum metallicity of a star is to be able to form planets of different masses. A good value to use for the mass of Saturn's terrestrial core is approximately 10 M_{Earth}. Therefore, for a star to be capable of producing a terrestrial core of this size, it would require its initial dust cloud to contain at least one-third the quantity of metals that are in our solar system. This corresponds to a metallicity of $[Fe/H] \geq -0.477$, which is marked in Figure 9 by a purple line. A similar calculation can be done for an earth-sized planet. A single 1 M_{Earth} object would require a metallicity of $[Fe/H] \geq -1.477$, which has been marked off on the same plot by a blue line.

Comparing these mass thresholds to the cumulative metallicity distribution shows that, carrying forward our assumption of dust cloud mass, it should be expected that the probability of finding a Saturn-like planet around a star in the galactic halo is minimal, as the fraction of stars even capable of forming such a planet is on the order of 5%. Earth-sized planets should be considered more likely, as we expect roughly 65% of stars in the galactic halo to be capable of their formation. Knowing this, we can limit our selection of stars for observation by exoplanet missions by first getting abundance profiles of potential targets, which will allow us to eliminate stars which have a low probability of having formed exoplanets.

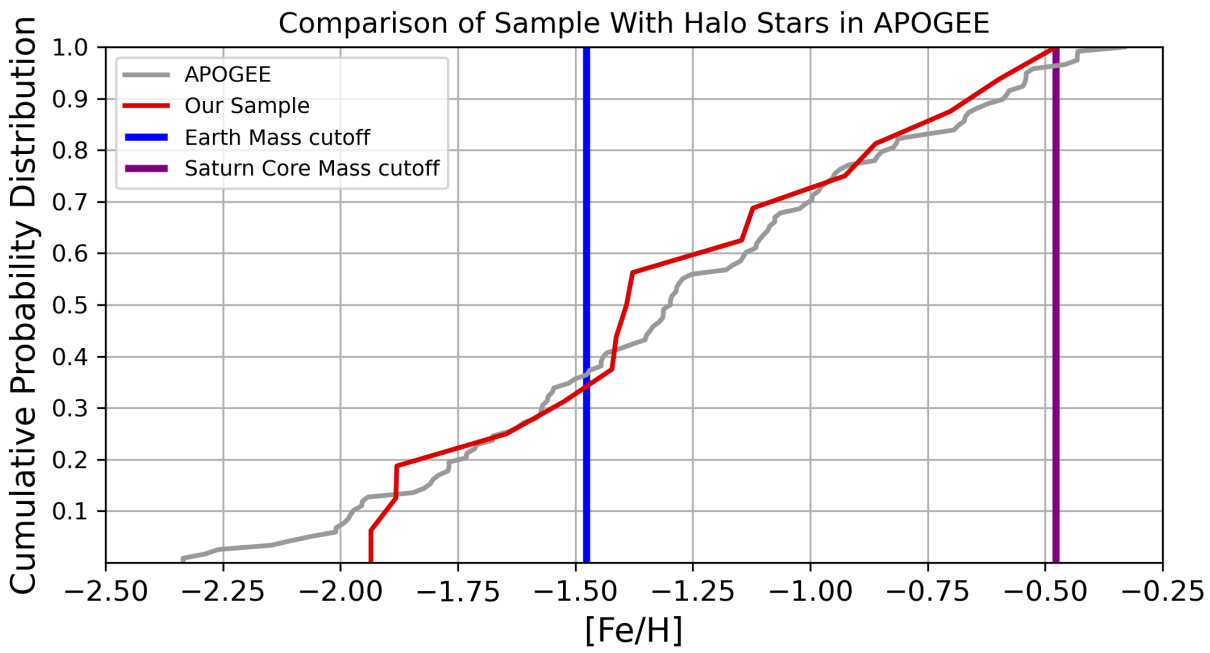

Figure 9: Addition of Mass Thresholds to Figure 7, Assuming Solar Dust Cloud Size

REFERENCES

Adamow, M. M. 2017, in American Astronomical Society Meeting Abstracts, Vol. 230, American Astronomical Society Meeting Abstracts #230, 216.07

Boesgaard, A. M., Rich, J. A., Levesque, E. M., & Bowler, B. P. 2011, ApJ, 743, 140, doi: 10.1088/0004-637X/743/2/140

Bullock, J. S., & Johnston, K. V. 2005, ApJ, 635, 931, doi: 10.1086/497422

Casey, A. R., Kennedy, G. M., Hartle, T. R., & Schlaufman, K. C. 2018, MNRAS, 478, 2812, doi: 10.1093/mnras/sty1208

Fulbright, J. P. 2000, AJ, 120, 1841, doi: 10.1086/301548

Gaia Collaboration, Prusti, T., de Bruijne, J. H. J., et al. 2016, A&A, 595, A1, doi: 10.1051/0004-6361/201629272

Johnson, D. R. H., & Soderblom, D. R. 1987, AJ, 93, 864, doi: 10.1086/114370

Muirhead, P. S., Dressing, C. D., Mann, A. W., et al. 2018, AJ, 155, 180

Palme, H., Lodders, K., & Jones, A. 2014, Solar System Abundances of the Elements, ed. A. M. Davis, Vol. 2, 15–36

Reddy, B. E., Lambert, D. L., & Allende Prieto, C. 2006, MNRAS, 367, 1329, doi: 10.1111/j.1365-2966.2006.10148.x

Sneden, C. 1973, ApJ, 184, 839, doi: 10.1086/152374

Stassun, K. G., Oelkers, R. J., Pepper, J., et al. 2018, AJ, 156, 102

Stassun, K. G., Oelkers, R. J., Paegert, M., et al. 2019, AJ, 158, 138

Table 3: Elemental Abundances Relative to Solar [dex]

Star	Fe II	Fe I	Li	Mg	Al	Si	Ca	Ti	V	Cr	Ni	Y	Ba	Eu
BD+18 3309	-1.524 ±0.043	-1.927 ±0.023	1.064 ±0.200	-1.776 ±0.261	–	-1.106 ±0.000	-1.444 ±0.016	-1.537 ±0.022	–	-1.940 ±0.016	-1.775 ±0.042	-1.642 ±0.030	-2.016 ±0.060	–
BD+18 3423	-0.861 ±0.026	-1.084 ±0.023	1.394 ±0.180	-1.128 ±0.209	–	-0.843 ±0.101	-0.908 ±0.028	-0.931 ±0.018	-1.150 ±0.220	-1.156 ±0.051	-1.174 ±0.017	-1.094 ±0.046	-1.027 ±0.030	–
BD+20 2594	-0.926 ±0.019	-1.072 ±0.025	1.259 ±0.130	-1.155 ±0.169	–	-0.872 ±0.030	-0.777 ±0.033	-0.801 ±0.010	–	-1.058 ±0.022	-1.089 ±0.018	-1.055 ±0.104	-0.998 ±0.050	–
BD+20 3603	-1.935 ±0.047	-2.161 ±0.019	1.431 ±0.160	-1.969 ±0.121	–	–	-1.774 ±0.002	–	–	-2.292 ±0.045	-2.179 ±0.060	–	–	–
BD+25 1981	-1.391 ±0.034	-1.582 ±0.019	–	-1.221 ±0.119	–	–	-1.078 ±0.054	-1.214 ±0.040	–	-1.602 ±0.028	-1.488 ±0.032	-1.282 ±0.059	-1.838 ±0.030	–
BD+34 2476	-1.880 ±0.034	-2.214 ±0.022	1.348 ±0.210	-1.669 ±0.493	–	–	-1.769 ±0.020	-1.409 ±0.020	–	-2.307 ±0.018	-2.172 ±0.060	–	-2.304 ±0.030	–
BD+36 2165	-1.422 ±0.024	-1.615 ±0.026	1.477 ±0.110	-1.704 ±0.132	–	-1.147 ±0.040	-1.099 ±0.142	-1.193 ±0.010	–	-1.614 ±0.126	-1.740 ±0.022	-0.841 ±0.701	-1.588 ±0.070	–
BD+42 2667	-1.378 ±0.022	-1.592 ±0.019	1.418 ±0.130	-1.629 ±0.153	–	-1.097 ±0.019	-1.193 ±0.018	-1.189 ±0.023	–	-1.630 ±0.037	-1.578 ±0.015	-1.381 ±0.040	-1.700 ±0.020	–
BD+51 1696	-1.413 ±0.030	-1.404 ±0.024	0.995 ±0.150	-1.440 ±0.136	–	-1.192 ±0.037	-1.129 ±0.032	-1.107 ±0.022	–	-1.433 ±0.025	-1.504 ±0.018	-1.586 ±0.080	-1.744 ±0.080	–
BD+72 659	-0.477 ±0.242	-0.930 ±0.034	–	-0.435 ±0.160	-0.361 ±0.030	0.434 ±0.080	-0.600 ±0.045	-0.474 ±0.117	-0.514 ±0.230	-0.884 ±0.035	-0.647 ±0.117	-0.231 ±0.348	-1.496 ±0.030	–
BD+75 839	-1.146 ±0.028	-1.273 ±0.023	1.077 ±0.140	-1.025 ±0.093	–	-1.065 ±0.122	-0.971 ±0.052	-0.971 ±0.014	-1.259 ±0.210	-1.213 ±0.010	-1.300 ±0.017	-1.328 ±0.064	-1.980 ±0.080	–
HD 64090	-1.882 ±0.060	-1.829 ±0.027	0.502 ±0.190	-1.500 ±0.143	–	–	-1.501 ±0.035	-1.437 ±0.011	-1.610 ±0.220	-1.849 ±0.027	-1.837 ±0.021	-1.967 ±0.115	-2.239 ±0.040	–
HD 108177	-1.646 ±0.037	-1.728 ±0.018	1.493 ±0.160	-1.449 ±0.206	–	–	-1.434 ±0.028	-1.269 ±0.032	–	-1.709 ±0.119	-1.751 ±0.018	-0.634 ±1.005	-1.960 ±0.030	–
HD 160693	-0.598 ±0.051	-0.867 ±0.041	–	-1.702 ±1.236	-0.380 ±0.013	-0.401 ±0.080	-0.489 ±0.032	-0.545 ±0.053	-0.614 ±0.230	-0.724 ±0.035	-0.708 ±0.023	-0.820 ±0.047	-1.005 ±0.050	–
HD 194598	-1.122 ±0.037	-1.239 ±0.027	1.440 ±0.140	-1.266 ±0.059	–	-0.954 ±0.085	-0.928 ±0.035	-0.991 ±0.044	–	-1.212 ±0.040	-1.302 ±0.042	-1.338 ±0.044	-1.275 ±0.070	–
TYC 3873-597-1	-0.702 ±0.037	-0.928 ±0.035	–	-1.774 ±1.071	-0.547 ±0.081	-0.545 ±0.091	-0.537 ±0.055	-0.507 ±0.029	-0.722 ±0.260	-0.780 ±0.017	-0.787 ±0.020	-1.021 ±0.154	-1.102 ±0.070	0.040 ±0.200